Performance of different techniques of generation and absorption of free-surface waves in Computational Fluid Dynamics

Young-Myung Choi, Young Jun Kim, Benjamin Bouscasse, Sopheak Seng, Lionel Gentaz, Pierre Ferrant

▶ **To cite this version:**

Young-Myung Choi, Young Jun Kim, Benjamin Bouscasse, Sopheak Seng, Lionel Gentaz, et al.. Performance of different techniques of generation and absorption of free-surface waves in Computational Fluid Dynamics. Ocean Engineering, 2020, 214, pp.107575 -. 10.1016/j.oceaneng.2020.107575 . hal-03491992

HAL Id: hal-03491992
https://hal.science/hal-03491992v1

Submitted on 22 Aug 2022

HAL is a multi-disciplinary open access archive for the deposit and dissemination of scientific research documents, whether they are published or not. The documents may come from teaching and research institutions in France or abroad, or from public or private research centers.

L'archive ouverte pluridisciplinaire **HAL**, est destinée au dépôt et à la diffusion de documents scientifiques de niveau recherche, publiés ou non, émanant des établissements d'enseignement et de recherche français ou étrangers, des laboratoires publics ou privés.

Distributed under a Creative Commons Attribution - NonCommercial 4.0 International License

Version of Record: https://www.sciencedirect.com/science/article/pii/S0029801820305837
Manuscript_d3e794533be840245c8c1f7f0dfa6e1b

Performance of different techniques of generation and absorption of free-surface waves in Computational Fluid Dynamics

Young-Myung Choi[a], Young Jun Kim[a,b], Benjamin Bouscasse[a,*], Sopheak Seng[b], Lionel Gentaz[a], Pierre Ferrant[a]

[a] *LHEEA Res. Dept., Ecole Centrale de Nantes and CNRS, Nantes, France*
[b] *Bureau Veritas, Paris, France*

Abstract

In wave-structure interaction problems, the minimization of wave reflection at boundaries is important for achieving accurate results and limiting the disturbances on the air/water interface. The present study compares a set of existing wave outlet techniques which are commonly applied in free surface simulations using a viscous flow solver. These techniques are stretched mesh, linear damping source, increased viscosity, and relaxation schemes. The comparisons are performed for test conditions which include propagation of regular incident waves and damping of radiation waves.

Keywords: Wave propagation, wave outlet, mesh stretching, damping source, viscosity outlet, relaxation, OpenFOAM
2010 MSC: 00-01, 99-00

1. Introduction

As computers become more and more powerful, Computational Fluid Dynamics (CFD) tools for solving free surface flows have gain more popularity within the naval and offshore engineering community. One common application is the analysis of wave-structure interactions. Typically ocean waves have periods in the range of $6 \sim 25$ s and they travel long distances with very small energy dissipation. For example, waves with a wavelength of 73.15 m ($T = 6.84\,s$) will travel 924 km in a day while their height only diminishes by one or two percent because of friction [1, 2]. For practical reasons the computational domain needs to be truncated to a manageable size. The far-field condition is replaced by wave outlet boundaries with specific numerical treatment in order to minimize reflection. Many numerical techniques have been developed to reduce wave reflection at these boundaries. The simplest approach is to stretch the mesh toward the

*Corresponding author
Email address: benjamin.bouscasse@ec-nantes.fr (Benjamin Bouscasse)

© 2020 published by Elsevier. This manuscript is made available under the CC BY NC user license
https://creativecommons.org/licenses/by-nc/4.0/

outlets which consequently yields varying performance depending on the configuration of the stretched mesh. Therefore it is attractive to develop more robust and efficient techniques. Israeli and Orszag (1981) showed that "damping zone" or "sponge layer" techniques, introducing a source term in governing equations, can be used to absorb waves effectively [3]. Another technique is to use a combination of linear and quadratic vertical velocity sources in the sponge layer (outlet zone) [4, 5, 6].

The numerical treatments of wave outlets are complicated by the existence of upstream propagated waves. These waves are usually generated by the interaction between waves and structure in the computational domain. As a consequence these scattering waves need to be absorbed at both inlet and outlet. Among the outlet techniques, the approach of relaxation schemes appear to be able to satisfy this need [7, 8, 9, 10, 11]. Here, the simulated waves are relaxed toward a given target in the sponge layer (also called relaxation zone or blending zone). The relaxation schemes can be further categorized into implicit and explicit relaxations. The implicit relaxation scheme adds equations for the target flow field to the governing equations using a spatially distributed weight function. As a result, source terms appear in the momentum equations [12, 11]. The explicit relaxation scheme performs the relaxation after solving the governing equations [7, 8, 9]. A comparative study of relaxation schemes with Dirichlet type boundary inlet-outlet and active wave absorption techniques can be found in [13, 14]. Higuera et al. (2013) reported with an active wave absorption technique wave reflection coefficients between 2% and 11% for a series of waves below 3% of wave height over wavelength ratio [13]. The Sommerfeld radiation condition, which can be viewed as a perfect non-reflecting boundary condition for regular linearized waves, has been applied at the outlet by [15]. It has been shown that the Sommerfeld radiation condition can be manipulated by approximation order at boundaries [15]. The higher-order Sommerfeld boundary conditions have been used by [16, 17] to force waves to propagate outside the boundary. In their approaches, an accurate evaluation of the varying phase velocity at the boundary is essential to minimize reflection. Duz et al. (2013) applied an approximated phase velocity with linearized Sommerfeld boundary condition in irregular wave simulation on staggered grids [18]. Later, Duz (2015) extended the Sommerfeld boundary condition up to second order [19]. As this condition is applied on the outlet boundary surface, the wave reflection obtained is relatively more sensitive to the case than when using relaxation schemes over the volumic domain. Other methods such as SWENSE (Spectral Wave Explicit Navier-Stokes Equations) can be applied to handle wave reflections in wave-structure interaction problems. With the SWENSE method the difficulty of propagating incident waves can be avoided. A comparative study with a similar solver as the one used in the present study can be found in [20].

The present study aims at comparing existing outlet conditions for propagating waves in OpenFOAM [21, 22, 23] (an open-source GPL license library mainly for solving partial differential equations using finite volume method). The third party toolbox known as `waves2Foam` [24] has been used for wave simulations and for the explicit wave relaxation scheme. First, a parametric

study of the solver, named `foamStar`, is conducted in order to design a proper numerical setting for wave propagation with a cyclic lateral condition. Then, two 2D test cases are proposed: a Numerical Wave Tank (NWT) with propagating incident waves, and a 2D radiation problem. Results using the explicit relaxation scheme with different target functions, mesh stretching techniques, linear damping source, and increased viscosity in the outlet are compared in the present study. Parametric studies are conducted for each outlet configuration. Note that non-reflecting conditions based on mathematical formulations applied at the domain boundary, such as the Sommerfeld condition, are not considered in the present study. In the present study, the 2D cases are only considered to minimize the complexity of computations and the number of parameters to be considered.

2. Numerical solver

`foamStar` is an in-house code co-developed by Bureau Veritas and Ecole Centrale de Nantes in the OpenFOAM framework for solving wave-structure interactions problems. It is based on the standard multi-phase solver `interDymFoam` in the OpenFOAM package [23, 25]. Two special modules are introduced for wave-structure interactions. The wave generation module is taken from `waves2Foam` and the mechanical solver is devised to solve the dynamics of rigid and flexible floating bodies in waves. Some examples of 3D wave generation of realistic sea spectrum can be found in [26].

2.1. Governing equations and solution algorithms

The fluid is assumed incompressible and the incompressible Navier-Stokes equations are applied to describe flow. The governing equations are written as

$$\nabla \cdot \mathbf{u} = 0 \tag{1}$$

and

$$\frac{\partial(\rho \mathbf{u})}{\partial t} + \nabla \cdot (\rho \mathbf{u}\mathbf{u}^T) - \nabla \cdot \left[\mu \left(\nabla \mathbf{u} + \nabla \mathbf{u}^T\right)\right] = -\nabla p_d - (\mathbf{g} \cdot \mathbf{x}) \nabla \rho \tag{2}$$

where $\mathbf{u}$, $\mathbf{x}$ and $\mathbf{g} = [0, 0 - g]^T$ are the fluid velocity, the position vector and gravitational acceleration vector, respectively. The dynamic pressure $p_d = p - \rho \mathbf{g} \cdot \mathbf{x}$ is introduced [23]. The mixture density ρ and viscosity μ are given as

$$\rho = \rho_w \alpha + \rho_a (1 - \alpha) \tag{3}$$

$$\mu = \mu_w \alpha + \mu_a (1 - \alpha) \tag{4}$$

where the subscript w and a represent water and air, respectively. α is the Volume of fluid (VOF) phase fraction. For $\alpha = 1$ the control volume (CV) is totally wet and for $\alpha = 0$ it is totally dry. The interface is inside the cell control volume where $\alpha = (0, 1)$. The transport equation for α is written as

$$\frac{\partial \alpha}{\partial t} + \nabla \cdot (\alpha \mathbf{u}) + c_\alpha \nabla \cdot (\mathbf{u}_n \alpha (1 - \alpha)) = 0 \tag{5}$$

where the third term on the left-hand-side is the artificial compression term to keep the interface sharp. $\mathbf{u}_n$ is the fluid velocity normal to the interface and c_α is the compression coefficient.

The solution algorithm of `foamStar` is shown in Fig. 1. In the time loop, the weight used to generate and absorb waves in the relaxation zone is updated. The governing equations and α-transport equation are solved in the PIMPLE loop (an implementation of combined SIMPLE and PISO algorithms supplied with OpenFOAM). The body motion is solved in a mechanical solver and the computational mesh is updated according to the displacement of the body-surface boundaries. After solving the α-transport equation, the relaxation scheme is applied to impose the target α-field in the relaxation zones. After solving the fluid velocity and pressure in the PISO algorithm, the fluid velocity is relaxed toward the prescribed target velocity field in the relaxation zone. In the present study, no turbulence model is considered. When it is required, however, the turbulence model is solved as the last step in the algorithm. Details of each step in the solution algorithm are described in [27].

2.2. Finite volume discretization and definition

The collocated second-order finite volume discretization is applied to the whole computational domain to solve the governing equations. The control volumes are arbitrary polyhedra with an example of the geometrical description of a computational cell with index P shown in Fig. 2 [22]. The volume is V_P. Each cell face is either a boundary face or an internal face which is connected to a neighbor cell of index N. The surface area of an arbitrary face f is represented in terms of a normal vector $\mathbf{S}_f$ where its magnitude is equal to the surface area. The distance from cell P to its neighbor N is denoted as vector $\mathbf{d}_f = \mathbf{x}_N - \mathbf{x}_P$.

2.3. Time integration scheme

A time integration scheme in OpenFOAM can be selected among Implicit Euler (`Euler`), Crank-Nicolson (`CN`), and second-order backward differentiation formula (`BDF2`). The supplied multiphase solver of OpenFOAM, `interDymFoam`, uses a special module which is called Multidimensional Universal Limiter with Explicit Solution (MULES) to solve the α-transport equation. MULES employs a method based on predictor and corrector steps to ensure α boundedness. As an example, when the `Euler` scheme is selected, the predictor step is as follows:

$$\frac{V_P^{n+1}\alpha_P^* - V_P^n \alpha_P^n}{\Delta t} + \sum_f^N F_{\alpha,f}^b = 0 \tag{6}$$

where the superscripts $*$ and n denote the predictor and time iteration, respectively. The time step between two successive time iterations is Δt. The equation flux is $F_{\alpha,f}^b$ where the superscript b denotes that the flux is bounded. To ensure the boundedness, $F_{\alpha,f}^b$ is computed in the predictor step using a 1st-order upwind scheme. The corrector step introduces a flux limiter λ_f such that

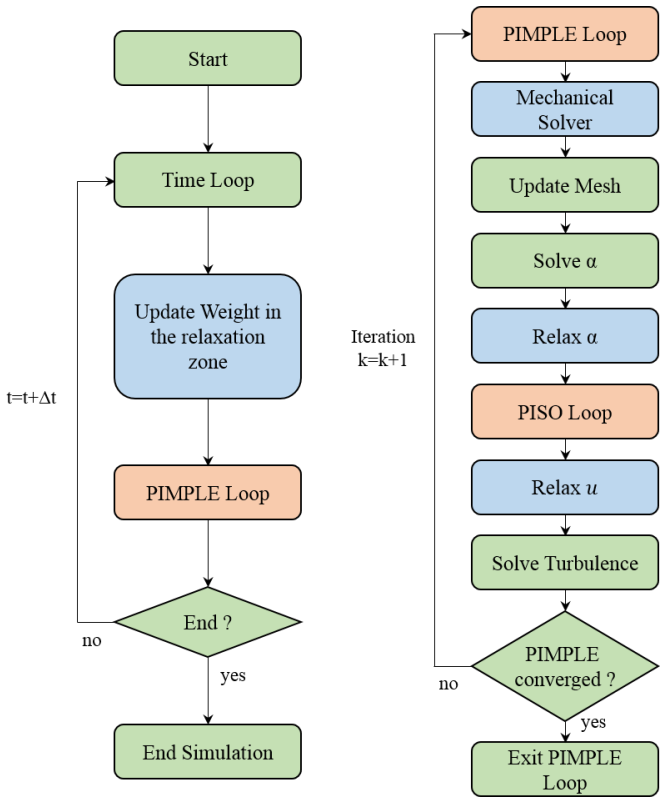

Figure 1: The computational algorithm of foamStar [27]

the correction for the high-order flux $F^u_{\alpha,f}$ does not cause unboundedness. The correction is as follows:

$$\frac{V_P^{n+1}\alpha_P^{n+1} - V_P^{n+1}\alpha_P^*}{\Delta t} + \sum_f \lambda_f (F^u_{\alpha,f} - F^b_{\alpha,f}) = 0. \tag{7}$$

The sum of equations (6) and (7) produces the original discretized α transport equation. In summary, the Crank-Nicolson scheme in MULES algorithm is a variation from the classical Crank-Nicolson scheme due to: the use of predictor and corrector steps; the existence of a flux limiter λ_f introduced to maximize the α transportation while keeping the α boundness. The MULES algorithm with the application of Crank-Nicolson scheme is given in Appendix A and a detailed description of the algorithm including MULES can be found in [25].

For the Crank-Nicolson time integration scheme the predictor and the corrector steps are formulated to account for the weight factor γ which exists in the classical formulation of the Crank-Nicolson. For $\gamma = 0$, the scheme is equivalent

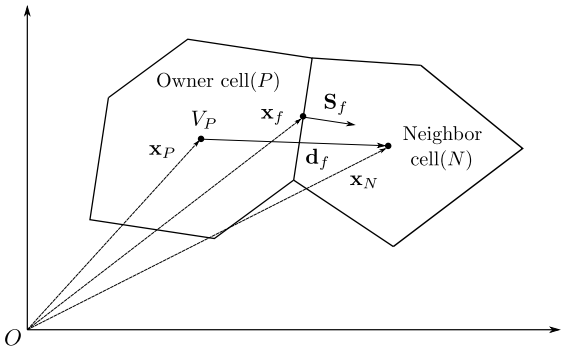

Figure 2: Geometrical description of a computational cell in the framework of OpenFOAM

to the explicit Euler integration scheme and for $\gamma = 1$ the resulting scheme is an implicit Euler time integration scheme. The classical formulation of the CN scheme requires $\gamma = \frac{1}{2}$. In OpenFOAM, the implementation allows γ to be selectable within a range of $\gamma \in \left[\frac{1}{2}, 1\right]$. To facilitate this selection, an off-center coefficient (hereafter called the Crank-Nicolson off-center coefficient; c_{CN}) is used instead of γ. The relation is

$$c_{CN} = \frac{1-\gamma}{\gamma}, \qquad c_{CN} \in [0, 1]. \tag{8}$$

where $c_{CN} = 0$ represents the implicit Euler integration, and $c_{CN} = 1$ represents the classical Crank-Nicolson scheme. It is commonly recommended to use $c_{CN} \approx 0.9$ as a compromise between stability and accuracy [28].

2.4. Remarks on the `V`-scheme in OpenFOAM

The treatment of the convection term in the Navier-Stokes equations affects the numerical dissipation and stability. One of the commonly used schemes is the second-order upwinding scheme. In OpenFOAM it is selectable either as `linearUpwind` or `linearUpwindV`. The latter is refered to as the `V`-scheme. Differences exist when the scheme is applied to a vector field. The `V`-scheme contains an additional limiter which is applied to all components of the vector field [28]. The numerical details concerning `linearUpwind` and `linearUpwindV` are outlined in the following. The finite volume discretization of the convection term reads

$$\iiint_{V_P} \nabla \cdot (\mathbf{uf}) dV \approx \sum_f^N (\mathbf{S}_f \cdot \mathbf{u}_f)(\mathbf{f})_f = \sum_f^N \phi_f (\mathbf{f})_f \tag{9}$$

where $\mathbf{f}$ is a vector field, $\mathbf{u}$ is the transport velocity, $(\mathbf{f})_f$ is the interpolated vector at the face center $\mathbf{x}_f$, the face vector $\mathbf{s}_f$ has the magnitude of the face area and the flux is $\phi_f = \mathbf{S}_f \cdot \mathbf{u}_f$. The index f represents the face index between cell P

and N. The computation of $(\mathbf{f})_f$ using the second-order upwinding scheme is as follows:

$$(\mathbf{f})_f = \mathbf{f}^{\text{upwind}} + \Delta\mathbf{f}^{\text{corr}} \tag{10}$$

where $\mathbf{f}^{\text{upwind}}$ is determined from the cell value in the upwinding direction using the sign of the flux:

$$\mathbf{f}^{\text{upwind}} = \begin{cases} \mathbf{f}_P, & \phi_f > 0 \\ \mathbf{f}_N, & \phi_f \leq 0 \end{cases} \tag{11}$$

The correction term $\Delta\mathbf{f}^{\text{corr}}$ differs when selecting `linearUpwind` or `linearUpwindV`. The `linearUpwind` scheme proceeds as follows:

$$\Delta\mathbf{f}^{\text{corr}} = \Delta\mathbf{f}_o^{\text{corr}} \tag{12}$$

where

$$\Delta\mathbf{f}_o^{\text{corr}} = \begin{cases} (\mathbf{x}_f - \mathbf{x}_P) \cdot (\nabla\mathbf{f})_P, & \phi_f > 0 \\ (\mathbf{x}_f - \mathbf{x}_N) \cdot (\nabla\mathbf{f})_N, & \phi_f \leq 0 \end{cases} \tag{13}$$

The gradients $(\nabla\mathbf{f})_P$ and $(\nabla\mathbf{f})_N$ are the cell averaged gradients computed separately by other means. The `V`-version of this scheme (i.e. `linearUpwindV`) contains an additional limiter:

$$\Delta\mathbf{f}^{\text{corr}} = \lambda_f^{\text{limiter}} \Delta\mathbf{f}_o^{\text{corr}} \tag{14}$$

where

$$\lambda_f^{\text{limiter}} = \min\left(1, \quad \frac{\Delta\mathbf{f}_o^{\text{corr}} \cdot \Delta\hat{\mathbf{f}}^{corr}}{|\Delta\mathbf{f}_o^{\text{corr}}|^2}\right) \tag{15}$$

with

$$\Delta\hat{\mathbf{f}}^{corr} = \begin{cases} (1-w)(\mathbf{f}_N - \mathbf{f}_P), & \phi_f > 0 \\ w(\mathbf{f}_P - \mathbf{f}_N), & \phi_f \leq 0 \end{cases} \tag{16}$$

where w is the distance weight corresponding to a central difference linear interpolation from cell-centered P and N to the shared face f. This linear interpolation is written as

$$(\mathbf{f})_f = w\mathbf{f}_P + (1-w)\mathbf{f}_N \tag{17}$$

The effect of $\lambda_f^{\text{limiter}}$ is to limit $(\mathbf{f})_f$ of Eq. (10) to be at most the same as Eq. (17).

3. Parametric study on wave propagation in a periodic domain

The parametric study is conducted with `foamStar` to find a proper numerical setting for propagation of a regular wave with properties given in Table 1. The simulations are performed in a two-dimensional domain with cyclic lateral boundary conditions. The free surface and the wave kinematics are initialized at the initial time from a fully nonlinear stream function wave solution [29]. The schematic view of the problem, the initialized phase-fraction field (VOF) and the computational mesh are shown in Fig. 3. The computational domain

Table 1: Wave condition for the parametric study

Item	Height (H)	Period (T)	Depth (h)	λ	H/λ
Unit	[m]	[s]	[m]	[m]	[-]
Value	0.0575	0.7018	0.6	0.8082	0.0712

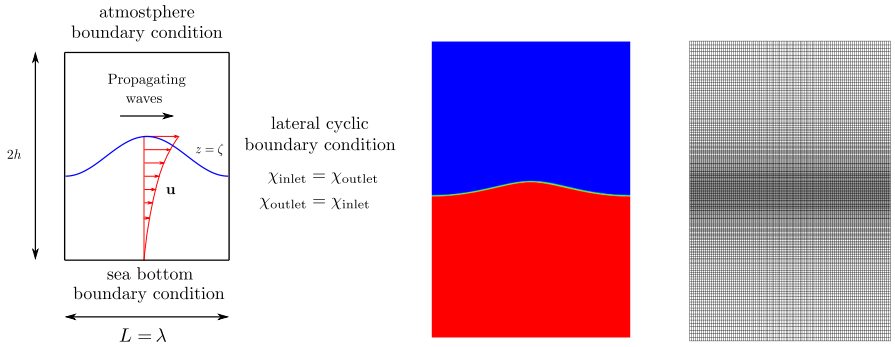

(a) Computational domain (b) Initialized α-field (c) Computational mesh

Figure 3: Schematic view on the parametric study of propagating waves with the cyclic lateral boundary conditions.

covers one wavelength ($L = \lambda$), and the height is taken to be two times the water-depth ($2h$; $h = 0.6m$). The computational meshes use a uniform cell distribution in the wave propagation direction with characteristic cell size of Δx. In the vertical direction, the cell distribution is specified in three zones: the air, the free surface and the underwater zone. Unless otherwise indicated, the free surface zone is limited to $z \in [-H, H]$ with a uniform cell distribution of size Δz in the vertical direction. The air zone is above the free surface zone ($z \in [H, h]$) and below is the underwater zone ($z \in [-h, -H]$). Cells outside the free surface zone are stretched perpendicularly from the free surface. The level of stretching is specified in term of a ratio between of Δz of the first and the last cells.

3.1. Effect of time scheme

Simulations were performed with Crank-Nicolson off-center coefficient $c_{CN} = 0$ (Euler implicit), 0.5 and 0.95 in order to observe the effect of the time integration scheme. The time step is kept constant at $\Delta t = T/400$, and mesh parameters are fixed to $\Delta x = \lambda/100$, $\Delta z = H/20$, and stretching ratio 5. Fig. 4 compares the simulated wave elevations at the center of the domain with those predicted by the stream function wave theory. Because the stream function wave theory provides a fully nonlinear solution of the potential flow waves, it is used here as a reference for the simulated results. Noticeably, the simulated wave amplitudes decrease gradually over time. The amount of the amplitude decays are better evaluated by applying the moving window Fast Fourier Transform (mwFFT) to time series [30]. The results are shown in Fig. 5 in terms

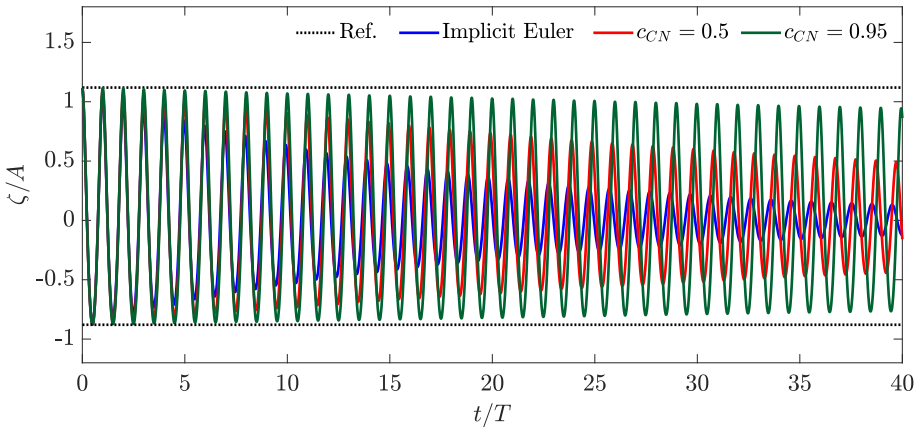

Figure 4: The measured wave elevation time series with respect to different Crank-Nicolson off-center coefficients

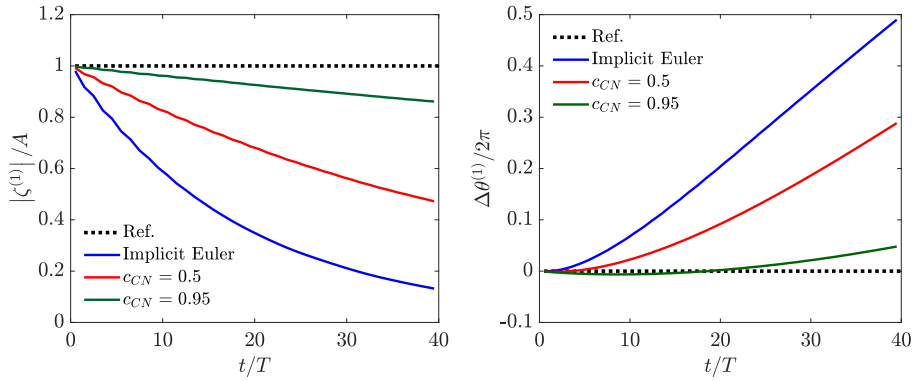

(a) Harmonic amplitudes (b) Phase differences

Figure 5: Comparison of first harmonic wave amplitudes and its phase differences with respect to Crank-Nicolson off-center coefficients (c_{CN})

of the first harmonics and the corresponding phases. The reference value, obtained from the potential flow theory, is denoted as "Ref." in Fig. 5. The phase differences between the CFD results and the stream function solution are significantly larger for the low-order time integration scheme. While the numerical errors in these simulations can be improved further through a refinement study, the present results show that for the same mesh parameters and same time step sizes one may benefit significantly from using a highly accurate time integration scheme. For the rest of the present study, the time integration scheme is set to Crank-Nicolson with $c_{CN} = 0.95$.

Table 2: Mesh and time discretizations for the convergence tests.

Case	$\lambda/\Delta x$	$H/\Delta z$	$T/\Delta t$	Co	Re_Δ
Mesh025-dt100	25	5	100	0.171	8836
Mesh050-dt200	50	10	200	0.171	4418
Mesh100-dt400	100	20	400	0.171	2209
Mesh200-dt800	200	40	800	0.171	1105
Mesh100-dt100	100	20	100	0.684	2209
Mesh100-dt200	100	20	200	0.342	2209
Mesh100-dt800	100	20	800	0.086	2209
Mesh100-dt1600	100	20	1600	0.043	2209

3.2. Mesh and time step convergence

The computational mesh and time steps are tested to obtain the formal convergence order of the discretization schemes. Mesh parameters are given in Table 2 in terms of lateral spacing Δx, vertical spacing in the free surface zone Δz, and time step Δt. The mesh stretching ratio in the air zone and in the underwater zone is kept constant at 5. Representative Courant number (Co) and cell-Reynolds number (Re_Δ) can be defined by using analytic wave fluid velocities as $\mathrm{Co} = \sqrt{\mathrm{Co}_x^2 + \mathrm{Co}_z^2}$ and $\mathrm{Re}_\Delta = \sqrt{\mathrm{Re}_{\Delta x}^2 + \mathrm{Re}_{\Delta z}^2}$ where,

$$\mathrm{Co}_x = \frac{u_{\mathrm{wave}}\Delta t}{\Delta x}, \quad \mathrm{Co}_z = \frac{w_{\mathrm{wave}}\Delta t}{\Delta z}, \quad \mathrm{Re}_{\Delta x} = \frac{u_{\mathrm{wave}}\Delta x}{\nu}, \quad \mathrm{Re}_{\Delta z} = \frac{w_{\mathrm{wave}}\Delta z}{\nu}$$

and u_{wave} and v_{wave} are the maximum horizontal and vertical fluid velocities given by stream function waves, respectively. The kinematic viscosity of water is denoted by ν. Two series of tests are conducted. The first series varies the cell size and consequently the cell-Reynolds numbers while the Courant number is fixed by varying accordingly the time steps. In the second series, the cell-Reynolds numbers are fixed and the Courant numbers are varied. Fig. 6 shows snapshots of velocity fields at time instants $t = 20T$ and $t = 40T$. The results using `V`-scheme remains smooth for at least $40T$. Between times $20T$ and $40T$ the distribution of the velocity field remains mostly unchanged with most visible differences in phases and the position of the crests. Without the `V`-scheme, the velocity field remains smooth for a shorter duration whereafter large spurious velocity appears in the vicinity of the free surface. Consequently, the free surface is very erroneous without using the `V`-scheme for a long simulation duration.

Amplitudes of the first harmonic of wave elevations at the center of the domain obtained over time for different Courant numbers and cell-Reynolds numbers are compared in Fig. 7. The results show that the additional limiter introduced in the `V`-scheme, Eq. (14), leads to larger numerical dissipation than in the case without applying the `V`-scheme. Without using the `V`-scheme, the high disturbance of the interface leads to a stong decrease of the wave amplitude for long simulations.

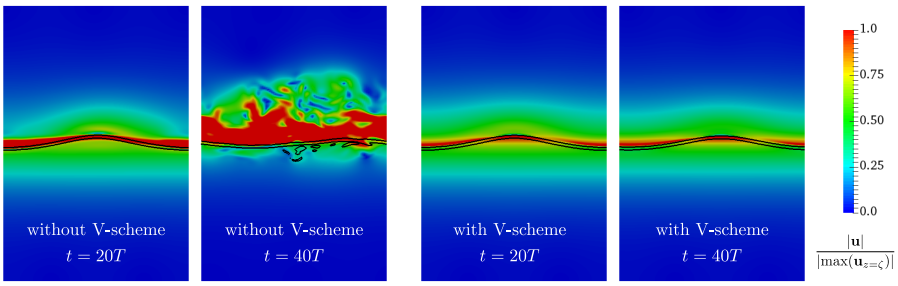

Figure 6: Snaphots of simulated velocity fields with/without the `V`-option in the convection scheme, black colored line denotes $\alpha = 0.01, 0.99$.

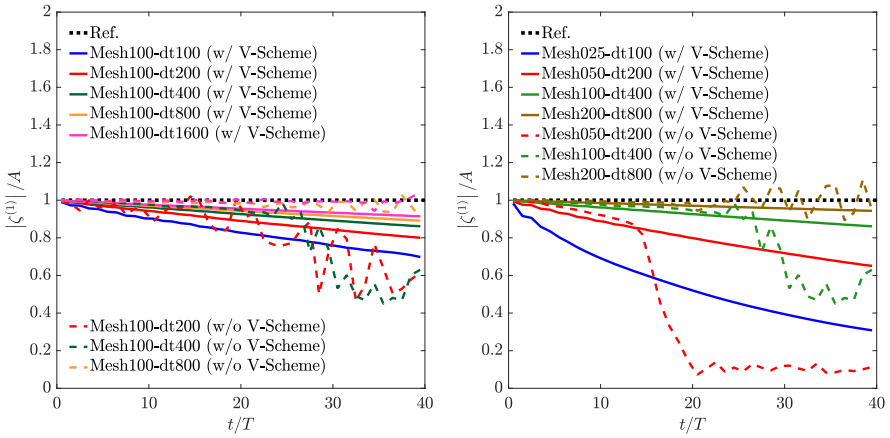

(a) Different Co (b) Different Re

Figure 7: Comparison of first harmonic wave amplitudes with different mesh and time discretizations (Simulation conditions are given in Table 2)

Before the large interface disturbance, errors of the first harmonics at $10T$ and $20T$ are shown in Table 3 for Mesh100-dt400 with and without the `V`-scheme. This mesh configuration (Table 2) corresponds to mesh parameters $\Delta x = \lambda/100$, $\Delta z = H/20$ and $\Delta t = T/400$. The representative Courant number is 0.171 and cell-Reynolds number is 2209. This shows that for short simulations, the `V`-scheme can lead to smaller wave amplitude.

The present results show that using the `V`-scheme is beneficial for a long simulation duration by reducing the interface disturbance. Applying `V`-scheme gives a slightly reduced wave amplitude, it is thought to be manageable and insignificant for a long simulation time.

Convergence analyses are performed for the first harmonics obtained during the first ten wave periods. The orders of convergence are computed according to the procedure of Eça and Hoekstra (2014) which applies a least square method to get the order of convergence (p) and the associated uncertainty estimation

Table 3: Errors of the first harmonics for Mesh100-dt400 (see Table 2)

t/T	w/o V-scheme	w/ V-scheme
10	2.33 %	3.84 %
20	5.55 %	7.41 %

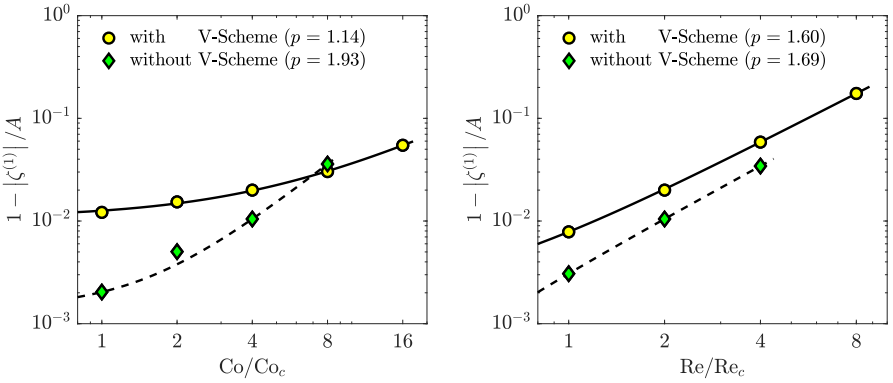

(a) Co discretization, $\mathrm{Co}_c = 0.043$ (b) Re discretization, $\mathrm{Re}_c = 1105$

Figure 8: The convergence orders and uncertainties with respect to discretization of Co and Re_Δ.

[31]. The results are shown in Fig. 8. The orders of convergence (p) for varying Courant and cell-Reynolds numbers and using the V-scheme are estimated to be 1.14 and 1.60, respectively. Without using the V-scheme, the estimated convergence order increases to 1.93 and 1.69.

Similar results are obtained by [32] where it is stated that the interface disturbance can appear with the use of higher-order schemes to capture a sharp interface between liquid and gas. They also showed that the choice of time-integration and convection schemes affect the interface shape and a combination of more or less diffusive schemes can improve the wave quality. However, the choice of more or less diffusive schemes depends on the case, therefore the upwind scheme which is reported as giving gradually decreasing amplitude but consistent results is selected in the present study. Further simulations are performed without the V-scheme while the results are evaluated with more emphasis on data up to $20T$.

3.3. Mesh spacing in vertical direction

In deep water, the velocity field of propagating waves has an exponential profile in the vertical direction under the free surface. According to the potential flow wave theory, the maximum velocity occurs at the free surface and it decays rapidly going away from the free surface. Therefore, in the vertical direction, meshes are generated using 3 zones: (1) underwater zone($z \in [-h, -H]$), (2) free surface zone($z \in [-H, H]$) and (3) air zone ($z \in [H, h]$). The cell resolution

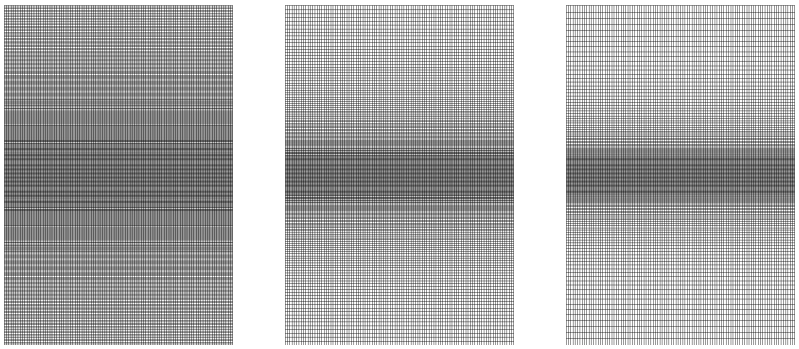

(a) Mesh-212 (b) Mesh-515(original) (c) Mesh-818

Figure 9: Different vertical mesh spacings of three divided zones with the geometric ratio.

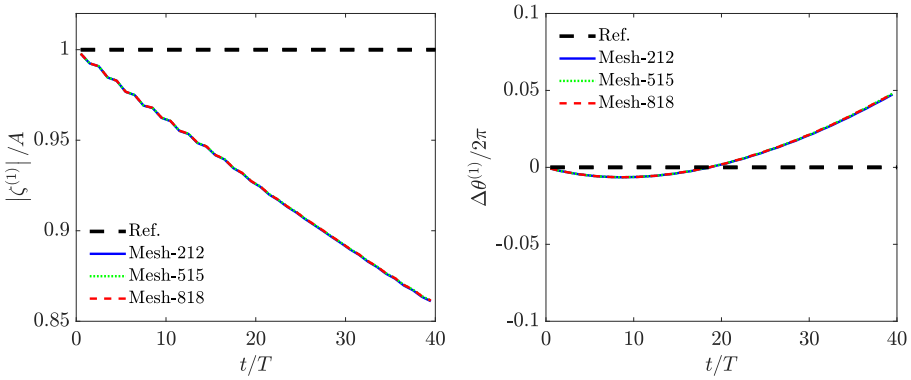

(a) Amplitude (b) Phase differences in radians

Figure 10: The first harmonic amplitudes and phase differences with respect to vertical mesh spacing.

is configured to be relatively dense inside and near the free surface zone and it is coarsened gradually towards the bottom. To study the effects of this coarsening, simulations are performed on several meshes with different stretching ratios. A naming scheme is chosen: `Mesh-ijk`, where i, j, and k represents the stretching ratio of zones: underwater, free surface and air, respectively. Here, the stretching ratio is defined as the ratio between the maximum and minimum cell height. Fig. 9 illustrates `Mesh-212`, `Mesh-515` and `Mesh-818`. The cells are uniformly distributed in the horizontal direction with $\Delta x = \lambda/100$ and within the the free surface zone with $\Delta z = H/20$. As seen in Fig. 10, the first harmonic amplitudes and the phases for all three meshes are almost identical. Therefore, the stretching ratio `Mesh-515` which is applied throughout this study is thought to be sufficient for the wave condition under consideration.

4. Inlet/outlet condition

4.1. Relaxation zones

The wave generation and absorption method of `foamStar` is based on an explicit scheme which relaxes the computed solution towards a given target flow field [7, 8, 9, 24, 10]. The scheme requires a weight function which varies between 0 and 1 in the relaxation zones. The relaxation is performed as follows:

$$\chi = (1 - w)\chi + w\chi^{Target} \tag{18}$$

where χ is the computed flow field (i.e. either the VOF-field or the velocity field), w is the weight function and χ^{Target} is the given target flow field. It shall be noted that there exists an implicit relaxation scheme which performs the relaxation directly in the governing equations [11, 12]. This study does not cover this implicit approach due to its unavailablity in `foamStar`. Hence, only the explicit relaxation scheme is considered.

The choice of the weight function w is important to minimize wave reflections. A discussion on smoothness criteria for w was originally presented in [9]. Two common choices can be identified: a polynomial weight function [7, 9], and an exponential weight function [7, 9, 24, 10]. Seng (2012) introduces further a dynamic weight function w_d defined as follows [10]:

$$w_d = 1 - (1 - w)^{\left|\mathbf{u}-\mathbf{u}^{Target}\right|\Delta t/\Delta x} \tag{19}$$

where w is the original static weight and Δx is the characteristic cell size [10]. The dynamic weight w_d is recomputed at every time step and is changed locally and adaptively based on the local differences between computed and target velocity. The relaxation proceeds as in Eq. (18) using w_d instead of w. The static weight function w remains either a polynomial or an exponential function:

$$w(\xi) = \begin{cases} \dfrac{e^{\xi^{3.5}} - 1}{e - 1}, & \text{exponential weight} \\ -2\xi^3 + 3\xi^2, & \text{polynomial weight} \end{cases} \tag{20}$$

where $\xi \in [0, 1]$ is a normalized coordinate in the relaxation zones. The present study evaluates the explicit relaxation scheme using either exponential or polynomial weight functions in combination with the static or the dynamic weight formulation. In addition, the evaluation covers various sizes of the relaxation zone which is considered as an important parameter to obtain an optimal compromise between the computational cost and the amount of the reflected waves. Miquel et al., (2018) reported $3 - 9\%$ of wave reflection for regular waves using an explicit relaxation scheme with static exponential function [14]. Perić and Abdel-Maksoud (2018) showed the wave reflection can be less than 1% for $L^{outlet} \geq 2\lambda$ when a strength of relaxation factor is optimized and applied to the exponential weight function [33].

The target function is another important parameter. When a floating or a fixed body exists within the incident wave field, radiation-diffraction waves

are generated due to interactions of the wave field with the body. In numerical computations using the relaxation schemes, the target flow field is usually set to be either the incident wave field or calm-water because the radiation-diffraction waves are unknown. Alternatively, the target wave field within the relaxation zones can be estimated from the observed wave elevations and kinematics in front of the outlet zone. When the wave amplitude decreases, the wavenumber changes due to a nonlinear effect which is proportional to $O\left((k_1 A)^3\right)$ in the third-order theory. For slightly smaller waves, the change of wavenumber is almost negligible. Therefore, it is assumed that the propagating waves do not change their wave frequency and wave number, the amplitudes and phases of the first harmonic of the observed waves are calculated using the Fourier transform for corresponding ω and k_1 as follows:

$$A' = \frac{2}{T\cos\Delta\phi}\int_{t-T}^{t}\zeta(x_0,\tau)\cos(k_1(x-x_0)-\omega\tau)d\tau \tag{21}$$

and

$$\tan(\Delta\phi) = -\frac{\int_{t-T}^{t}\zeta(x_0,\tau)\sin(k_1(x-x_0)-\omega\tau)d\tau}{\int_{t-T}^{t}\zeta(x_0,\tau)\cos(k_1(x-x_0)-\omega\tau)d\tau} \tag{22}$$

where A' is the amplitude of the first harmonic of the modified waves, $\Delta\phi$ is the phase between the incident and the modified waves and $\zeta(x_0,\tau)$ is the measured wave elevation in front of outlet zone at x_0. The modal wavenumber k_1 is obtained from nonlinear stream function theory [34]. Wave elevations and fluid velocities of the modified waves are then given by

$$\zeta = \frac{A'}{A}\left[\frac{a_0}{2}+\sum_{n=1}^{N_a}a_n\cos(k_n x-\omega t+\Delta\phi)\right] \tag{23}$$

$$\mathbf{u} = \nabla\times[0,-\psi,0]^T \tag{24}$$

$$\psi = \frac{A'}{A}\times\left[b_0 z+\sum_{n=1}^{N_b}b_n\frac{\sinh k_n(z+H)}{\cosh k_n H}\cos(k_n x-\omega t+\Delta\phi)\right] \tag{25}$$

where N_a and N_b are the numbers of truncated Fourier modes of stream function waves and a_n and b_n are the amplitudes of the Fourier mode for wave elevation and for stream function, respectively. k_n are the wavenumber. Details can be found in [29, 34].

4.2. Sponge layer method

Alternatively, the addition of linear and quadratic damping source terms to the momentum equations can be used to damp waves [4, 6]. The approach is known as a sponge layer method and was originally proposed by [3]. The momentum equations with the source terms are

$$\frac{\partial(\rho\mathbf{u})}{\partial t}+\nabla\cdot(\rho\mathbf{u}\mathbf{u}^T)-\nabla\cdot\left[\mu\left(\nabla\mathbf{u}+\nabla\mathbf{u}^T\right)\right] = -\nabla p_d-(\mathbf{g}\cdot\mathbf{x})\nabla\rho+\mathbf{S} \tag{26}$$

where μ is a dynamic viscosity, $p_d = p - \rho \mathbf{g} \cdot \mathbf{x}$ is the dynamic pressure. The source terms $\mathbf{S}$ include both the linear and quadratic damping sources and are formulated to be applied to the vertical velocity components as follows:

$$\mathbf{S} = [0, 0, \rho(C_1 + C_2 u_z) w u_z]^T \tag{27}$$

where w is the weight function; C_1 and C_2 are the linear and quadratic damping coefficients, respectively. Through a parametric study, Perić and Abdel-Maksoud (2016) reported wave reflection coefficients of less than 1% thanks to an optimal choice of alternatively C_1 or C_2 [6]. They proposed a practical recommendation for the simulation with exponential weight function and the condition $L^{outlet} \geq 2\lambda$. In the present study, only the linear damping is considered with polynomial weight function. Hence, C_2 is set to zero.

4.3. Other alternatives

Two other alternatives for wave damping are considered in this study due to their simplicity: the mesh stretching and the increased viscosity. Mesh stretching introduces the desired wave damping and also additional dispersive effects. The increased viscosity is a method where the viscosity is increased artificially in the outlet zone. Wave damping occurs due to the increased energy loss caused by the artificial viscosity. The momentum equation with increased viscosity in the outlet is written as

$$\frac{\partial(\rho \mathbf{u})}{\partial t} + \nabla \cdot (\rho \mathbf{u}\mathbf{u}^T) - \nabla \cdot \left[(\mu + \mu_{add}) \left(\nabla \mathbf{u} + \nabla \mathbf{u}^T \right) \right] = -\nabla p_d - (\mathbf{g} \cdot \mathbf{x}) \nabla \rho \tag{28}$$

where μ_{add} is the increased viscosity in the outlet zone.

5. Outlet study I: Numerical Wave Tank (NWT)

The aim is to assess the quality of waves in a numerical wave tank as a prerequisite to perform a successful simulation involving wave-structure interactions. Consequently the size of the domain is chosen to be representative of typical cases and the quality of the simulated waves is assessed in time.

5.1. Reflection coefficients

Waves simulated in numerical wave tanks are affected by the numerical dissipation, the free surface instabilities, and the performance of the wave absorption method at the outlet. The latter is often characterised through the use of a wave reflection coefficient, which is defined as the ratio of amplitudes of propagating and reflecting waves at steady state. For small wave amplitudes, the wave reflection coefficient is defined as in [35]:

$$C_R = \frac{a_{\max} - a_{\min}}{a_{\max} + a_{\min}} \tag{29}$$

where $a_{\max}$ and $a_{\min}$ are the maxima and minima of the wave envelope amplitude. This definition works well for linear waves. With no reflection, the

amplitude modulation of the linear wave goes to zero. Hence, $a_{\max} = a_{\min}$ and the reflection coefficient becomes $C_R = 0$. When the linear waves are fully reflected, the amplitude envelope has $a_{\min} = 0$. Therefore, the reflection coefficient becomes $C_R = 1$. However, wave conditions used in the present study are nonlinear and the above definition is no longer sufficient. Perić and Abdel-Maksoud (2016) used the same definition as shown in Eq. (29) but the amplitude is replaced by the wave height [6]. The reflection coefficient Eq. (29) can be computed based on the first-order amplitudes ignoring the higher harmonics, i.e. by means of the fast-Fourier transform (FFT). This definition was used in [36, 37, 38] to quantify the reflection coefficient when the wave field is at quasi-steady state. In the present study, the reflection coefficient is evaluated with first-harmonic amplitude as in associated researches [36, 37, 38], but the FFT is performed within a moving window in time to better capture the transient nature of the present simulations. Given data within a window of one period, the time-varying first harmonics at i-th wave gauge is computed as

$$a_i(\omega, t) = \frac{2}{T} \int_{t-T}^{t} \zeta(x_i, t) \cos(kx_i - \omega\tau) d\tau \tag{30}$$

where the subscript i denotes i-th wave gauge. The present simulations contain 250 wave gauges distributed over 5λ centered within the inner zone, Fig. 11.

The original definition of the wave reflection coefficient C_R as in 29 is introduced with the assumption that the propagating and reflected waves are fully established and no wave re-reflections are travelling back in the interval of interest. Therefore, the time and spatial intervals selection should not affect the result of the C_R coefficient. However, considering the domain length and the simulation duration considered in the present case, the re-reflection may appear before the reflected waves are fully propagated and generally time-varying wave amplitudes will occur during the simulation with also interface disturbance which may appear affecting the results. Consequently, the *coefficient of accumulated wave reflection* is introduced in the present study to observe the accumulated wave reflection over the simulation time. This coefficient can still be used to assess the quality in time of the waves observed in the domain. The *coefficient of accumulated wave reflection*, $\kappa_R(t)$, is defined using the first-harmonic amplitudes obtained in (30):

$$\kappa_R(t) = \frac{\max[a_i(t)] - \min[a_i(t)]}{\max[a_i(t)] + \min[a_i(t)]}. \tag{31}$$

5.2. Description of the case

The selected wave condition is as shown in Table 1 with the length of the domain set as in Fig. 11. The inlet relaxation zone is 1.5λ and 7λ is reserved for the inner zone where waves are propagated according to the governing equations. The outlet relaxation zones vary between 0.5λ to 6λ such that the coefficients of accumulated wave reflection at various lengths of the outlet can be studied. The vertical mesh spacing is `Mesh-515`. Waves are generated at the inlet boundary

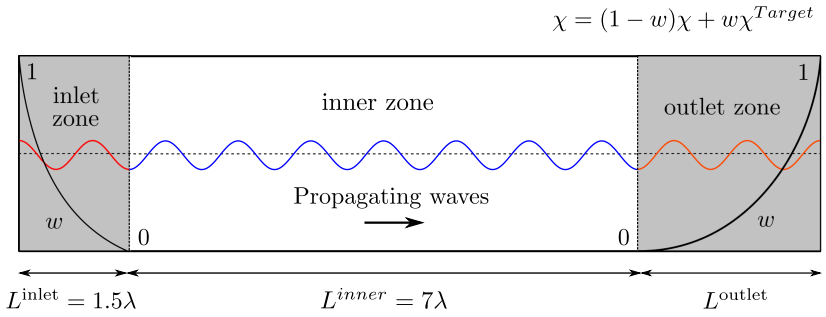

Figure 11: Schematic view of the NWT for a parametric study on the relaxation schemes. Several cases are generated for outlets of length between 0.5λ to 6λ.

and within the inlet relaxation zone based on the nonlinear solution (up to 15th order) of the stream function wave theory. In total, 250 wave gauges are uniformly distributed over 5λ centered within the inner zone (Fig. 11). Hence, the first and last wave gauges are located 1λ away from inlet and outlet zones, respectively. Free surface elevations read from these wave gauges are used in the evaluation of $\kappa_R(t)$ as described previously in Section 5.1. It is to be expected that the simulated waves while propagating through out the computational domain may see their amplitude and phase vary due to numerical dissipation. Consequently, the evaluation of $\kappa_R(t)$ may have some dependency on the selected distribution of the wave gauges. Theoretically, wave gauges shall cover at least 2λ in order to properly detect the complete envelope of the standing waves. The nature of this dependency, however, is not studied in this paper.

5.3. Results of using relaxation schemes

Four combinations of weight functions: static-exponential, static-polynomial, dynamic-exponential and dynamic-polynomial are studied implementing Eqs. (18) to (20). Various lengths of the outlet ($L^{\text{outlet}} = 1.5\lambda$, 3λ and 6λ) are considered for each of the four weight functions. In this parametric study the target function in inlet and outlet is set to be the incident waves computed with stream function theory.

The resulting maximum Courant numbers Co_{max} are shown in Fig. 12. This number is associated with the interface disturbance because velocity spikes happen around the free surface. Simulations with dynamic polynomial weight (Fig. 12d) have a less varying and lower maximum Co_{max} than those with other choices for all cases with $L_{outlet} \geq 1.5\lambda$. Furthermore, Co_{max} is less sensitive to the length of relaxation zones though a significant change occurs after approximately $20T$ for the outlet of 0.5λ. The results of the static and dynamic exponential weight functions give varying but similar Co_{max} evolution for $t \leq 20T$. Beyond this time, the results show that using a large outlet zone does not necessarily reduce Co_{max}. Overall, the maximum Courant number obtained using static polynomial weight is the highest.

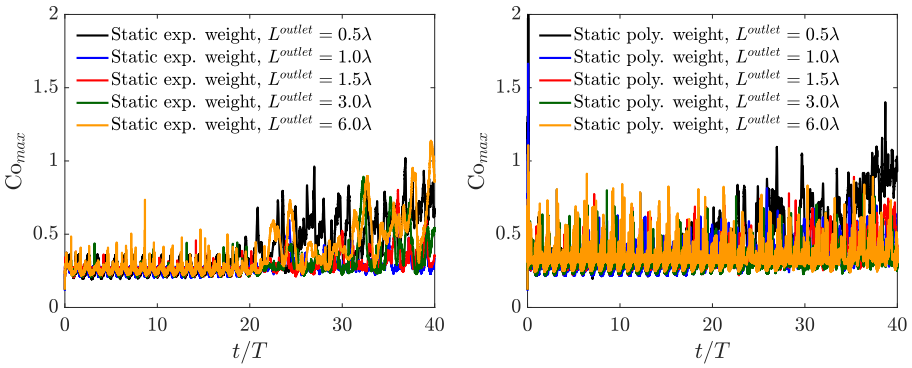

(a) Static exponential weight

(b) Static polynomial weight

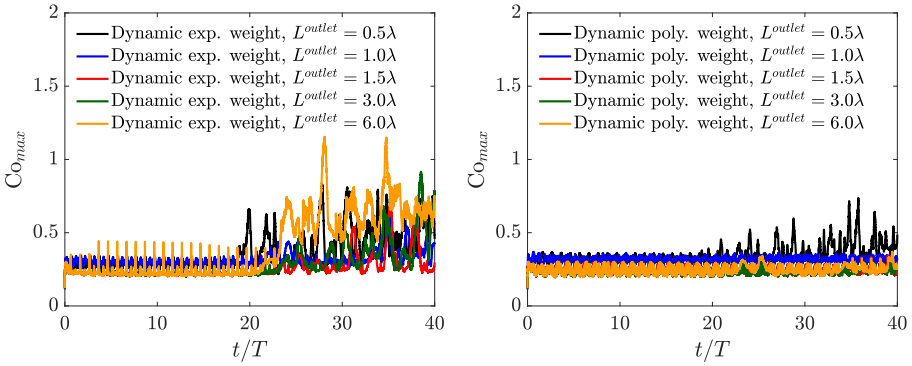

(c) Dynamic exponential weight

(d) Dynamic polynomial weight

Figure 12: Maximum Courant numbers read from the entire computational domain in cases where waves within the outlet zone is relaxed toward the stream function wave solution

The coefficients of accumulated wave reflection for different relaxation schemes and various lengths of the outlet are compared in Fig. 13. It appears that $\kappa_R(t)$ generally is increasing until approximately $t = 20T$. Reducing the lengths of the outlet zones from 1.5λ to 0.5λ increases κ_R. Beyond $20T$, the growth seems saturated with variations due to the interface disturbance. Using the dynamic polynomial weight with outlets of length greater than 1.5λ gives the smallest variation of κ_R in time.

Fig. 14 shows $\kappa_R(t)$ and the first harmonic amplitudes averaged over the simulation time $t \in [15T, 20T]$. Fig. 14a clearly shows that $\kappa_R(t)$ increases significantly for outlets of length smaller than 1λ. As presented in Fig. 14b, the first harmonic amplitudes obtained with static weights are closest to the reference value computed with the nonlinear stream function theory [34]. Specifically, the averaged first harmonic amplitude obtained from the cases $L_{outlet} \geq 1.5\lambda$ using the dynamic weight and the static weight are respectively 3.5% and 2.2% less than the reference value.

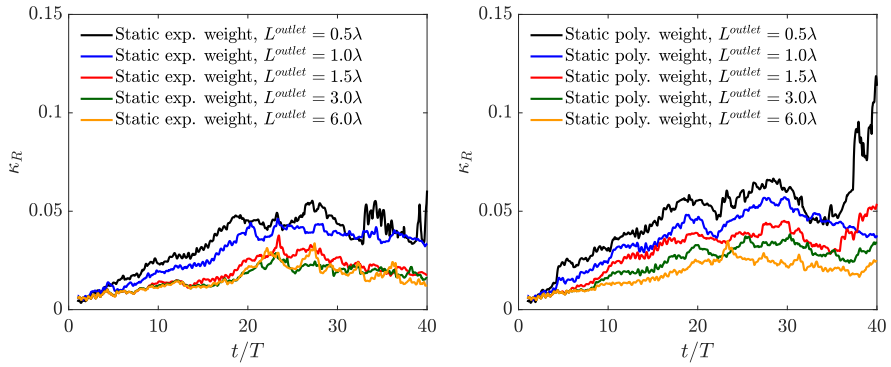

(a) Static exponential weight

(b) Static polynomial weight

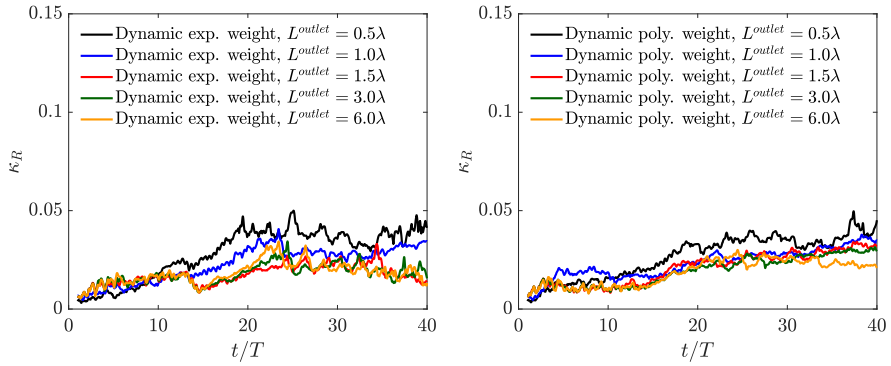

(c) Dynamic exponential weight

(d) Dynamic polynomial weight

Figure 13: Comparison of $\kappa_R(t)$ with respect to different relaxation schemes and lengths of the outlet

To summarize, even though the dynamic weight function gives slightly smaller wave amplitude (around 1% less), the wave reflection is reduced so as the interface disturbances. This is the setup chosen for comparison using relaxation zones in the last section. The results demonstrate strengths and weaknesses of each combination of static, dynamic, exponential and polynomial weights used in an explicit wave relaxation scheme.

5.4. Results of using stretched meshes

It is difficult to find a set of common parameters to generate stretched meshes for wave propagations because the resulting damping properties may depend strongly on the selected numerical schemes, the time step size and specific mesh setups and configurations [39, 40]. For the purpose of the present study, mesh stretching is performed length-wise in the propagation direction using a stretching ratio (r_x) defined as

$$\Delta x_n = r_x \Delta x_{n-1} \tag{32}$$

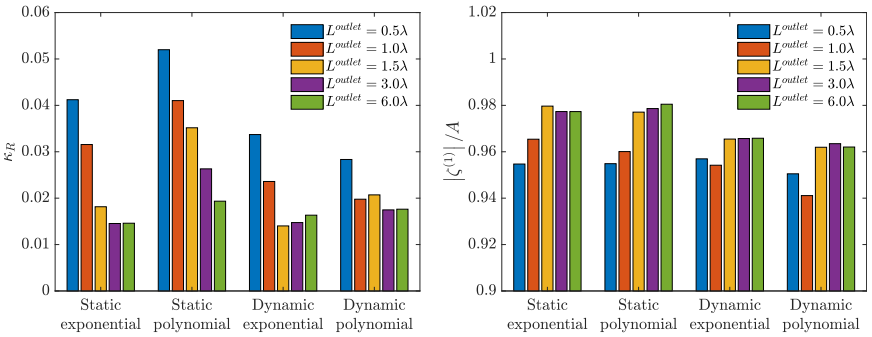

(a) Time-averaged coefficients of accumulated wave reflection

(b) Time-averaged first harmonic amplitudes

Figure 14: Comparison of averaged wave amplitudes and $\kappa_R(t)$ in $t \in [15T, 20T]$

Table 4: Information of stretched mesh outlet for propagating waves.

Choice of r_x	Number of cells	L/λ	$L^{\text{outlet}}/\lambda$	$\Delta x^{max}/\lambda$
$\gamma = 1.001$	225,420	39.6	31.1	1.11
$r_x = 1.02$	206,340	59.5	58.0	1.05
$r_x = 1.05$	180,120	29.9	21.4	1.14
$r_x = 1.08$	173,470	22.0	13.5	1.18

where Δx represents the longitudinal length of the cell and the subscripts n and $n-1$ indicate the intermediate neighbours. Two types of stretching are considered: the constant and the exponential stretching.

$$r_x = \begin{cases} c, & \text{constant stretching; } c = 1.02,\ 1.05 \text{ and } 1.08 \\ \cosh(\gamma n), & \text{exponential stretching; } \gamma = 1.001 \end{cases} \tag{33}$$

Cells within the outlet zone are stretched until the length of the last three cells is larger than one wavelength ($\Delta x \geq 1\lambda$). The properties of stretched mesh outlets are summarized in Table 4. The amount of stretching is visualized in Fig. 15. In particular, the exponential stretching yields a significantly denser distribution on one side of the outlet zone. In principle, the dense size is located at the start of the outlet zone and the mesh is stretched so that cells are increased in size in the propagation direction toward the end of the outlet zone. Table 5 shows time-averaged $\kappa_R(t)$ over $t \in [15T, 20T]$ at selected stretching ratios. The constant ratio of $r_x = 1.02$ gives the smallest time-average of $\kappa_R(t)$. Hence, it is selected to be representative for the stretched mesh outlet when comparing with other numerical outlets.

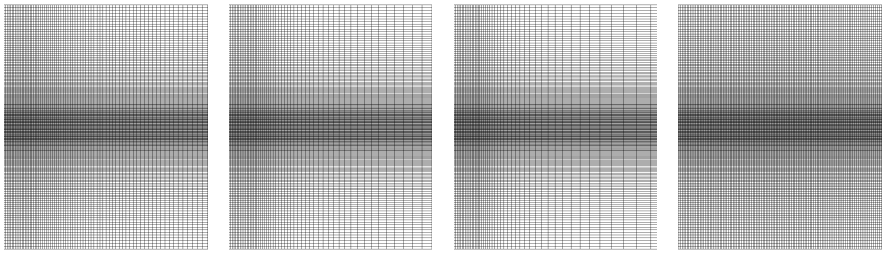

(a) $r_x = 1.02$ (b) $r_x = 1.05$ (c) $r_x = 1.08$ (d) $\gamma = 1.001$

Figure 15: Meshes near to the outlet with different stretching.

Table 5: The coefficients of accumulated wave reflection with respect to stretched mesh outlets, time averaged values over $t \in [15T, 20]$.

Choice of r_x	$\gamma = 1.001$	$r_x = 1.02$	$r_x = 1.05$	$r_x = 1.08$
κ_R	0.0311	0.0286	0.0334	0.0361

Table 6: The coefficients of accumulated wave reflection obtained using the linear damping source outlet over $t \in [15T, 20T]$.

L^{outlet}	C_1				
	30	20	10	5	1
1.5λ	0.0373	0.0287	0.0268	0.0936	-
3.0λ	-	0.0202	0.0196	0.0226	-
6.0λ	-	-	0.0199	0.0190	0.0190

5.5. Results of using a linear damping source outlet

Perić and Abdel-Maksoud (2016) showed that there is a need to appropriately define the damping coefficient to obtain an optimal wave absorption [6]. The authors used a Froude scaling law to find a dependency of damping coefficients and showed that the linear and quadratic damping coefficients could be scaled by wave frequency and wavelength, respectively. A static exponential weight function was used in the outlet and the recommendation is to use a linear damping coefficient, $C_1 = \pi\omega \approx 28.1$. They proposed a method to estimate $\kappa_R(t)$ by analyzing the wave equation with respect to the use of the linear damping source. Applied to the present wave condition, the algorithm predicts that the optimal linear coefficient for outlet of length 1.5λ is $C_1 \approx 7.5$ and the estimated C_R is 1.5%. It is noted that the algorithm assumes that the wave field is damped towards calm-water in the outlet zone and the weight is the static exponential function. Shen et al. (2016) used the linear damping coefficient of $C_1 = 20$ with a second order polynomial weight function for irregular wave simulations [41]. In the present study, the linear damping coefficient with cubic polynomial weight given in equation (20) is studied with different lengths of the outlet, Table 6. The present results show that for the outlet of length $L^{outlet} = 1.5\lambda$, using $C_1 = 10$ yields the lowest $\kappa_R(t)$. Hence, this result is selected to be representative for the use of linear damping source outlet. It should be remarked that the weight function considered in the present study is different from previous studies [6, 41], consequently it is able to make a difference.

5.6. Results of using increased viscous outlet

The increased viscous outlet imposes an artificially high viscosity in the outlet zone. For a smooth change of viscosity, the added viscosity μ_{add} is multiplied by the cubic polynomial weight function given in equation (20). Three different added viscosities are considered with the values $\mu_{add} = 0.5, 0.2$ and 0.1 kg.m^{-1}.s^{-1}, respectively. The resulting coefficients of accumulated wave reflection at various lengths of the outlet are given in Table 7.

5.7. Comparison and Discussion

The final comparison is done using several types of outlets: stretched mesh, linear damping source, increased viscosity and relaxation schemes changing the target wave field. The latter is set in turn to calm water, incident waves, and

Table 7: Coefficients of accumulated wave reflection with respect to the increased viscous damp outlet.

L^{outlet}	$\mu_{add}[kg \cdot m^{-1} \cdot s^{-1}]$		
	0.5 $(500\mu_{water})$	0.2 $(200\mu_{water})$	0.1 $(100\mu_{water})$
1.5λ	0.0668	0.0470	0.0205
3.0λ	0.0315	0.0388	0.0254
6.0λ	0.0298	0.0391	0.0241

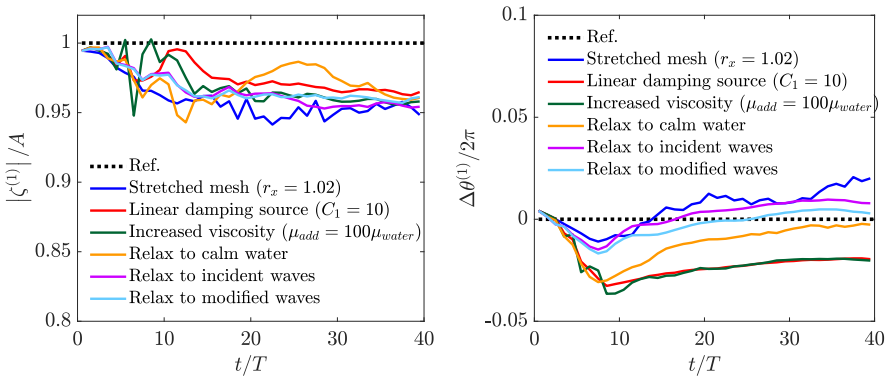

(a) Amplitude (b) Phase differences

Figure 16: Amplitudes and phases of the first harmonic of free surface elevations at the center of the computational domain.

to the modified waves described in an earlier section. The representative setup and results obtained from the parametric study for each outlet are used in the comparison. The comparison is limited to the outlet length $L^{outlet} = 1.5\lambda$ except for mesh stretching where the outlet is stretched as discussed in the dedicated section.

The time evolutions of the wave first harmonic amplitude and phase difference to the reference solution are presented in Fig. 16. The maximum errors with respect to the reference amplitude computed over 40 wave periods are below 7%. Amplitude modulations over the simulation time exists for all cases but are smaller for relaxation schemes which target the incident waves and the modified waves. Errors in the phase are around 3% using linear damping source and increased viscosity outlets. However, phase differences are smaller with the relaxation scheme outlets, around 1%. It appears that the phase difference is slowly approaching zero for the relaxation scheme using calm water as target fields.

The coefficients of accumulated wave reflection for the different outlets tested are plotted in Fig. 17. Initially, large $\kappa_R(t)$ are observed for linear damping, increased viscosity, and relax-to-calm-water outlets. This indicates that these outlets have an immediate effect on the initialized incident wave field. After the

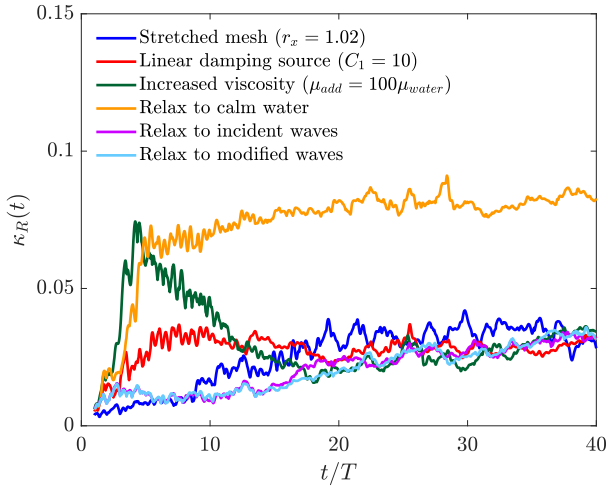

Figure 17: Evolution of $\kappa_R(t)$ for different outlets.

Table 8: Time-averaged coefficients of accumulated wave reflection $E[\kappa_R]$ computed over various time intervals.

Outlet	$E[\kappa_R(t/T \in [a,b])]$		
	$[15,20]$	$[25,30]$	$[35,40]$
Stretched mesh ($r_x = 1.02$)	0.029	0.034	0.033
Linear damping source ($C_1 = 10$)	0.027	0.034	0.037
Increased viscosity ($\mu_{add} = 100\mu_{water}$)	0.021	0.029	0.034
Relax to calm water	0.078	0.082	0.083
Relax to incident waves	0.020	0.029	0.032
Relax to modified waves	0.017	0.029	0.033

initial disturbance, $\kappa_R(t)$ increases during the whole simulation with relax-to-calm-water outlet, however $\kappa_R(t)$ obtained from simulations with linear damping and increased viscosity decreases toward a level similar to that of relax-to-waves outlets (from $t = 22T$). $\kappa_R(t)$ gradually increases over simulation time with mesh stretching outlet and relax-to-incident/modified-waves outlets.

These results show that it is important to use an appropriate target wave field in the relaxation zones. When the target wave field differs from the flow entering the outlet, the wave reflection becomes apparent.

The averages of $\kappa_R(t)$ computed over three distincts time intervals are tabulated in Table 8. In the time duration $t/T \in [15,20]$ which is before the appearance of large interface disturbance, the smallest $\kappa_R(t)$ is obtained for relax-to-modified-waves. Apart from relax-to-calm-water, all approaches gives $\kappa_R(t)$ of about $2-3\%$ over $t \in [15T, 20T]$. The accumulated wave reflection coefficients in the present study are similar to the wave reflection coefficients obtained by using static exponential weight function in [14]. Perić and Abdel-

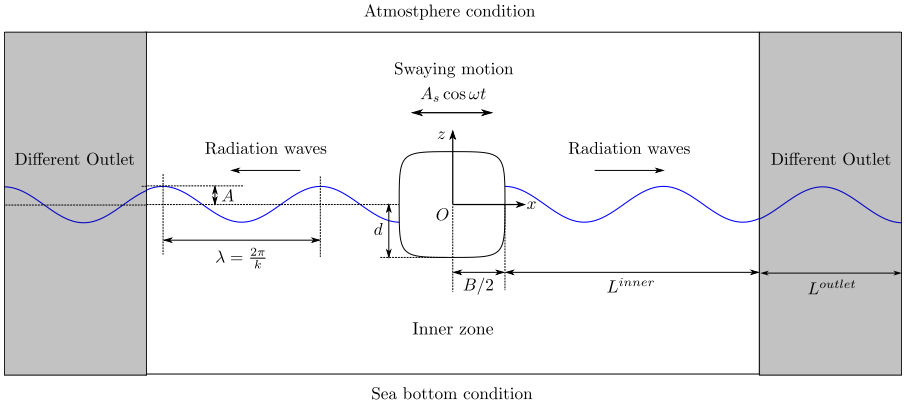

Figure 18: A schematic view of swaying Lewis form with different outlets.

Maksoud [33] showed that the wave reflection can be less than $\approx 1\%$ introducing a strength factor of relaxation.

The results shown here confirm that all wave outlet techniques can give acceptable results if they are properly used. Outlet techniques using a linear damping source or an increased viscosity require a tuning step on parameters. These parameters are C_1 for the linear damping source outlet and μ_{add} for the increased viscosity outlet. Although [6] provides a means to estimate optimal values of C_1 or C_2 the proper tuning of these additional parameters still represents additional work which must be performed on a case-by-case basis. Meanwhile, minimizing the wave reflection with the relaxation scheme requires a parametric study on the weight function for a specific simulation condition. Though the relax-to-incident-waves outlet gives the best results, it should be considered to be case specific because out-going waves are here expected to be the incident waves. Therefore this finding cannot be generalized to other cases where out-going waves contain expected disturbances, e.g., in the presence of a body and consequent radiation-diffraction waves the performance of this target function may differ. On the other hand, the relax-to-calm-water outlet is expected to give a performance consistent with what is shown in the present study.

6. Outlet study II: Radiation waves

6.1. Description

A swaying Lewis form in a two-dimensional domain is introduced to study the effect of relaxation schemes and to compare different outlets. A schematic view of the setup with different outlets is depicted in Fig. 18. In the middle of the domain, the Lewis form moves harmonically at amplitude A_s and frequency ω. The mesh is moving rigidly with the Lewis form without deformation. Hence, the initial mesh quality is preserved during the whole simulation.

Table 9: Selected sway frequencies and amplitudes for the Lewis form

Item	Frequency (ω)		
	2.4 rad/s	4.2 rad/s	7.0 rad/s
Swaying amplitude (A_s)	0.118 m	0.055 m	0.025 m
Wavelength (λ)	10.70 m	3.494 m	1.258 m
Wave amplitude (A)	0.102 m	0.089 m	0.050 m
Wave steepness (kA)	0.06	0.16	0.25

The underwater offset of the Lewis form is given as

$$x = M\left\{(1+a_1)\sin\theta - a_3\sin 3\theta\right\} \tag{34a}$$

$$z = -M\left\{(1-a_1)\cos\theta + a_3\cos 3\theta\right\} \tag{34b}$$

with

$$a_1 = \frac{H_0 - 1}{2(M/d)}, \qquad a_3 = \frac{H_0 + 1}{2(M/d)} - 1$$

$$\frac{M}{d} = \frac{3(H_0+1) - \sqrt{(H_0+1)^2 + 8H_0(1-4\sigma/\pi)}}{4}$$

where x, z and $\theta \in= [-\pi/2, \pi/2]$ are the underwater offsets and the corresponding angle [42]; M is a magnification factor; B and d are breadth and draft, respectively; $H_0 = \frac{B/2}{d}$ and $\sigma = \frac{S}{Bd}$ are a ratio of half breadth to draft and an area coefficient corresponding to the block coefficient of a ship. The geometric coefficients of Lewis form used in this study are $B/2 = 1.0$ m, $d = 1.0$ m and $\sigma = 0.95$. The offset above the free surface is generated by mirroring with respect to $z = 0$. Sway motions at different frequencies and amplitudes have been considered, Table 9. These amplitudes are selected such that the resulting radiation waves estimated at far-field have lengths, heights and steepness which are suitable for a finite volume method discretization. Meshes are generated using the standard OpenFOAM meshing tool, `snappyHexMesh`, with refinements in x- and z-directions matching $\lambda/\Delta x \geq 100$ and $H/\Delta z \geq 20$. Local split-hex refinements near the body surface are applied up to level 4. An example of the computational meshes with $L^{outlet} = 2.5\lambda$ is shown in Fig. 19.

6.2. Comparison of different outlets

From the results of the previous parametric study, parameters $r_x = 1.02$, $C_1 = 20$ and $\mu_{add} = 100\,\mu_{water}$ are selected for mesh stretching, linear damping source and increased viscosity outlets, respectively. The target functions of relaxation schemes are set to either calm water or linear potential flow. The latter is available by Ursell-Tasai's multipole expansion [43, 44, 45] with Wheeler stretching. To determine the dependency on the size of inner and outlet zones, the relaxation schemes are firstly tested with different zone sizes. The considered domain sizes are given in Table 10. The domains are constructed between $z \in [-d - 0.75\lambda, 2\,d]$ with the length of outlet and inner zones scaled relatively

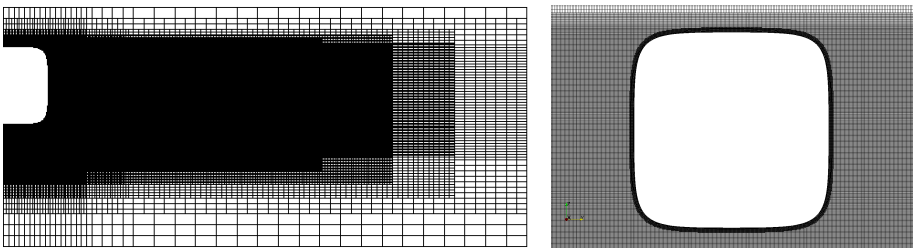

(a) One half of the total computational domain (b) Mesh near the body

Figure 19: An example of the computational meshes for harmonically swaying 2D Lewis form $\omega = 4.2\,rad/s$, $L^{inner} = 1\lambda$ and $L^{outlet} = 2.5\lambda$.

Table 10: Different domain sizes and meshes which are considered in the present study

		$\omega =$	$2.4\,rad/s$	$4.2\,rad/s$	$7.0\,rad/s$
Mesh name	L^{inner}	L^{outlet}	N_{cell}	N_{cell}	N_{cell}
P150R35	1.5λ	3.5λ	317,094	350,024	202,022
P100R35	1.0λ	3.5λ	273,996	313,784	172,666
P050R35	0.5λ	3.5λ	239,802	277,738	136,892
P025R35	0.25λ	3.5λ	219,020	254,010	131,968
P100R25	1λ	2.5λ	291,678	320,090	173,736
P100R20	1λ	2.0λ	283,824	323,276	174,260
P100R15	1λ	1.5λ	270,782	308,766	160,890

to the expected wavelength. Cells near the body surface are kept at a similar size for all cases. Pressure force on the body surface is recorded at each time step and added mass and radiation damping are extracted by Fourier transforms. Normalized added mass a'_{22} and radiation damping b'_{22} coefficients are computed as follows:

$$a'_{22} = \frac{a_{22}}{\rho(B/2)^2}, \qquad b'_{22} = \frac{b_{22}}{\rho\omega(B/2)^2} \tag{35}$$

where a_{22} and b_{22} are the added mass and radiation damping defined by

$$\frac{1}{T}\int_{t-T}^{t} F_2(\tau)e^{i\omega\tau}d\tau = A_s(\omega^2 a_{22} + i\omega b_{22}), \tag{36}$$

where $F_2(\tau)$ is the horizontal force and T is period. An example of a'_{22} and b'_{22} for frequency $\omega = 4.2\,rad/s$ using mesh P100R25 (i.e. $L^{inner} = 1\lambda, L^{outlet} = 2.5\lambda$) is shown in Fig. 20. It is noticeable that the radiation forces converge on average 1.6 times faster when the target function of the relaxation scheme is set to the known potential flow solution. The result which is labeled "Long-CFD-domain" is obtained on a mesh with the inner zone set to $L^{inner} = 12.5\lambda$. This size corresponds to approximately $20\,c_g T$ where $c_g = \frac{d\omega}{dk}$ is the group velocity. The outlet zone for this mesh is set to $L^{outlet} = 5\lambda$. The steepness (kA) of the

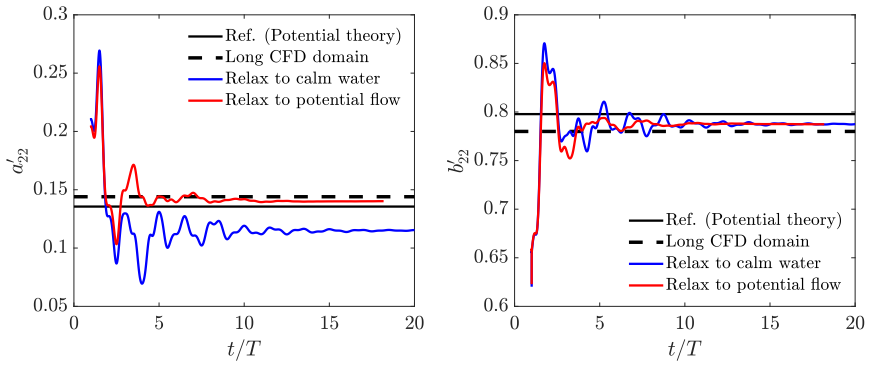

(a) Normalized added mass (b) Normalized radiation damping

Figure 20: Time series of normalized radiation added mass and damping using the relaxation scheme with the target flow set to either calm water or potential flow solution: The mesh is P100R25 (see Table 10) with $L^{inner} = 1\lambda$, $L_{outlet} = 2.5\lambda$ and $\omega = 4.2\,rad/s$.

radiation waves are expected to vary between 0.06 and 0.25 which are in the range of nonlinear waves. Hence, due to this nonlinearity the computed radiation forces may deviate from the linear potential flow solution. The result of Long-CFD-Domain is used here as a second reference in the comparison between the different outlets and domain sizes. The results are summarized in Table 11 where it can be seen that the deviations between linear potential flow solution and the results of the Long-CFD-Domain become larger as the wave steepness increases. The relative deviations as shown in Table 11 are computed as follows:

$$\text{Rel. dev.}\,[\%] := 100\frac{\left|\text{Computed} - \text{Ref.}\right|}{\text{Ref.}} \tag{37}$$

where "Ref." is the linear potential flow solution and "Computed" is the simulated data of e.g. the Long-CFD-Domain. The average of these relative deviations among the three frequencies are shown in Fig. 21 where it can be observed that the results of the relax-to-calm-water are approaching the results of the Long-CFD-Domain. The radiation forces are not so sensitive to the size of the inner zone and the relative differences between relax-to-calm-water and relax-to-potential-flow are in the range of deviations of the Long-CFD-Domain.

With respect to different outlets a relative comparison can be made from tabulated data in Table 12. The increased viscosity outlet ($\mu_{add} = 100\,\mu_{water}$) does not damp the radiation waves sufficiently and the time series of the radiation forces have modulation which increases dramatically due to reflection. These are marked as "-" in Table 12. It appears that the increased viscosity outlet may not be sufficiently good to treat the out-going waves without having its parameters tuned specifically for the particular case and for the wave frequency under consideration. Fig. 21c,d shows that the relative deviations for all outlets can be improved by increasing the size of the outlet zone. Clearly,

Table 11: Radiation force coefficients obtained from using various domain sizes (Table 10) with target function set to calm water. The relative deviation is as defined in Eq. (37).

Coef.	a'_{22}			b'_{22}		
ω $[rad/s]$	2.4	4.2	7.0	2.4	4.2	7.0
kA	0.06	0.16	0.25	0.06	0.16	0.25
Potential theory	1.304	0.136	0.365	2.169	0.798	0.156
Long CFD domain	1.297	0.144	0.388	2.162	0.780	0.148
Rel. deviation [%]	0.54	5.88	6.30	0.32	2.26	5.13
P150R35	1.279	0.129	0.386	2.190	0.779	0.146
P100R35	1.283	0.129	0.380	2.194	0.781	0.146
P050R35	1.278	0.129	0.391	2.192	0.781	0.146
P025R35	1.312	0.146	0.382	2.136	0.743	0.140
P100R25	1.281	0.115	0.375	2.194	0.788	0.149
P100R20	1.276	0.103	0.372	2.209	0.802	0.154
P100R15	1.276	0.096	0.368	2.248	0.832	0.162

Table 12: Radiation coefficients which are obtained by using different outlets (the mesh is P100R20 where $L^{inner} = 1.0\lambda$ and $L^{outlet} = 2.0\lambda$)

Coef.	a'_{22}			b'_{22}		
ω $[rad/s]$	2.4	4.2	7.0	2.4	4.2	7.0
Relax to calm water	1.276	0.103	0.372	2.209	0.802	0.154
Relax to potential flow	1.316	0.141	0.392	2.185	0.798	0.151
Linear damping source	1.270	0.121	0.384	2.263	0.782	0.148
Increased viscosity	-	0.154	0.388	-	0.842	0.147

the resulting radiation forces are more sensitive to the size of the outlet zone rather than to the size of the inner zone. If the relaxation scheme is applied with a target function very close to the actual outgoing waves, the size of inner and outlet zones can be reduced.

7. Conclusion

Different methodologies for wave outlets (relaxation zones with various target functions, damping layer, mesh stretching) are compared using two numerical setups. All tests are run on collocated unstructured finite volume method meshes. The first numerical setup tests the propagation and absorption of a regular wave and the second aims at computing radiation forces exerted on a harmonically surging Lewis form. Each of the outlets needs specific input parameters so dedicated parametric studies are conducted.

For the wave propagation case, a first parametric study with periodic domain confirms that a time integration scheme of second-order accuracy is necessary to maintain the wave amplitude for a long duration. It also shows that introducing an additional flux limiter with the `V`-scheme in OpenFOAM, gives more

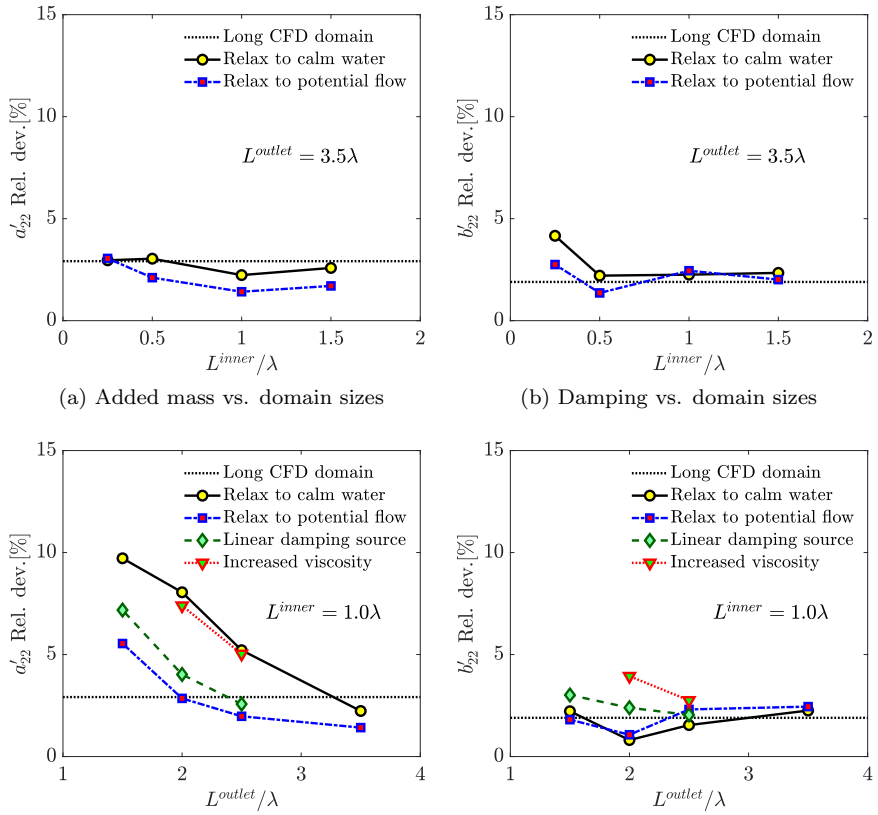

(a) Added mass vs. domain sizes

(b) Damping vs. domain sizes

(c) Added mass vs. outlet sizes

(d) Damping vs. outlet sizes

Figure 21: Relative deviations with respect to the linear potential flow solution. The presented data is averaged among the three frequencies in consideration.

dissipation but less disturbance on the interface, which is beneficial for the wave propagation simulation over long time. The first test case used for comparing outlet performances consists in propagating regular waves from inlet to outlet through a 7 wavelengths long domain where only the two-phase Navier-Stokes equations apply. The assessment of the wave quality is done comparing the first harmonic amplitude of the simulated waves with the fully nonlinear solution obtained from stream function theory and through a newly introduced coefficient of accumulated reflection. The study shows that if the different outlets are tuned properly the coefficients of accumulated wave reflection obtained are similar and about 3 %.

The use of a relaxation scheme with the explicit dynamic polynomial weight gives a robust and consistent result with sufficiently large size of outlet compared with other relaxation scheme for considered problem. However, it should be noted that the measured wave amplitude in the inner zone with application

dynamic polynomial weight has less amplitude than the case with static exponential weight which is important for a practical case. The wave reflection increases if the target fields in the outlet are very different from the solution entering the outlet with relaxation scheme (variation from 8 % using calm water to 1.7 % using tuned solution). The results obtained are also relevant in showing interface disturbance issues for simulation durations larger than 20 periods.

In the second numerical setup, the computed radiation forces on the swaying Lewis form provide an indicator for how much the computational domain can be reduced when using the different outlets. Similarly to what is shown in the wave propagation case, the parametric study performed with various domain sizes and the outlet length confirms that a convergence towards known references (both analytic solution from linear potential flow model and numerical results with large computational domain) can be obtained for all outlet methodologies if the input parameters are properly tuned and the size of the outlet zone is sufficiently large. With the relaxation scheme method, setting the target function close to the actual outgoing waves reduces considerably both the number of steps to achieve steady state and the length of the outlet zone, consequently saving simulation time.

Acknowledgements

This work has been performed in the framework of the Chaire Hydrodynamique et Structures Marines Centrale Nantes - Bureau Veritas. The authors are grateful to the anonymous referees whose valuable suggestions and comments significantly improved the quality of the paper.

Appendix A. Crank-Nicolson time scheme with MULES

The Multidimensional Universal Limiter with Explicit Solution (MULES) algorithm based on the FCT (Flux Corrected Transport) technique is used in OpenFOAM to solve the Volume of Fluid (VOF; α) transport equation [25, 46]. The application of the Crank-Nicolson scheme to the discretized α-transport equation in the Finite Volume method (FV) with second-order accuracy yields

$$\frac{(V_P\alpha_P)^{n+1} - (V_P\alpha_P)^n}{\Delta t} + \sum_f \left[C_n F^{n+1}_{\alpha,f} + (1 - C_n) F^n_{\alpha,f} \right] = 0. \tag{A.1}$$

where the superscript n represents the value at n-th time step, the subscript P represents the owner cell, V and f are the cell volume and faces surrounding the cell, respectively. C_n is computed from the Crank-Nicolson coefficient $c_{CN} = (1 - C_n)/C_n$, $c_{CN} \in [0, 1]$ where $(c_{CN} = 0; C_n = 1)$ and $(c_{CN} = 1; C_n = 0.5)$ represent the implicit Euler and classical Crank-Nicolson time scheme, respectively. $F_{\alpha,f} = \alpha\phi_f$ ($\phi_f = \mathbf{S}_f \cdot \mathbf{u}_f$) is the α flux defined at the face f. In MULES algorithm, equation (A.1) is solved in two steps: (1) *predictor* and (2) *corrector*.

In the *predictor* step, the predicted α^* is introduced with the implicit Euler time scheme and bounded flux which is ensured from the low order convection scheme, usually taken as the first-order upwind scheme:

$$\frac{(V_P\alpha_P)^* - (V_P\alpha_P)^n}{\Delta t} + \sum_f F^b_{\alpha^*,f} = 0 \tag{A.2}$$

where the superscript * represents the value in the *predictor* step and $F^b_{\alpha^*,f}$ is the bounded α flux.

In the *corrector* step, the α-transport equation is solved iteratively with the corrected flux as follows:

$$\frac{(V_P\alpha_P)^{**} - (V_P\alpha_P)^*}{\Delta t} + \sum_f \lambda_f \left[F^{CN}_{\alpha,f} - F^b_{\alpha^*,f}\right] = 0 \tag{A.3}$$

with

$$F^{CN}_{\alpha,f} = C_n F^{n+1}_{\alpha,f} + (1 - C_n)F^n_{\alpha,f} \tag{A.4}$$

In the equation (A.3), $F^{CN}_{\alpha,f} - F^b_{\alpha^*,f}$ represents the flux contribution from higher-order scheme. The flux limiter $\lambda_f \in [0, 1]$ is computed from α^* in the predictor step, or in the previous corrector step if the iterative correction is considered. The corrector step can be solved iteratively by updating $\alpha^* = (\alpha^{**})_{prev}$ and the bounded flux $F^b_{\alpha^*,f} = (F^b_{\alpha^*,f})_{prev} + (\lambda_f)_{prev}(F^{CN}_{\alpha,f} - F^b_{\alpha^*,f})_{prev}$ where the subscript $(\cdot)_{prev}$ represents the previous corrector step. After the corrector step, α^{n+1} is taken from the α^{**}.

The computed α^{n+1} from the MULES algorithm can be different with α^{n+1} from the classical Crank-Nicolson scheme given in (A.1) due to the existence of flux limiter λ_f which introduced to maximize the α-transportation while keeping the boundness.

References

[1] H. Lamb, Hydrodynamics, Dover Books on Physics, Dover publications, 1945.

[2] D. D. Joseph, Potential flow of viscous fluids: Historical notes, Int. J. of Multiphase Flow 32 (3) (2006) 285 – 310.

[3] M. Israeli, S. Orszag, Approximation of radiation boundary conditions, J. of Comp. Physics 41 (1) (1981) 115–135.

[4] J.-C. Park, M.-H. Kim, H. Miyata, Fully non-linear free-surface simulations by a 3D viscous numerical wave tank, Int. J. for Num. Methods in Fluids 29 (6) (1999) 685–703.

[5] J. Choi, S. Yoon, Numerical simulations using momentum source wave-maker applied to RANS equation model, Coastal Eng. 56 (10) (2009) 1043–1060.

[6] R. Perić, M. Abdel-Maksoud, Reliable damping of free-surface waves in numerical simulations, Ship Tech. Research 63 (1) (2016) 1–13.

[7] S. Mayer, A. Garapon, L. S. Sørensen, A fractional step method for unsteady free-surface flow with applications to non-linear wave dynamics, Int. J. for Num. Methods in Fluids 28 (1998) 295–315.

[8] D. R. Fuhrman, Numerical solutions of Boussinesq equations for fully nonlinear and extremely dispersive water waves, Ph.D. thesis, Technical University of Denmark, Kgs. Lyngby (2004).

[9] A. P. Engsig-Karup, Unstructured nodal DG-FEM solution of high-order Boussinesq-type equations, Ph.D. thesis, Technical University of Denmark, Kgs. Lyngby (2006).

[10] S. Seng, Slamming and whipping analysis of ships, Ph.D. thesis, Technical University of Denmark, Kgs. Lyngby (2012).

[11] V. Vukčević, Numerical modelling of coupling potential and viscous flow for marine applications, Ph.D. thesis, University of Zagreb (2016).

[12] J. Kim, J. O'Sullivan, A. Read, Ringing analysis of a vertical cylinder by euler overlay method, 31st Int. C. on Ocean, Offshore and Arctic Eng. (2012) OMAE2012–44915.

[13] P. Higuera, J. L. Lara, I. J. Losada, Realistic wave generation and active wave absorption for Navier-Stokes models: Application to OpenFOAM®, Coastal Engineering 71 (2013) 102 – 118. doi:https://doi.org/10.1016/j.coastaleng.2012.07.002.

[14] A. M. Miquel, A. Kamath, M. Alagan Chella, R. Archetti, H. Bihs, Analysis of different methods for wave generation and absorption in a CFD-based numerical wave tank, Journal of Marine Science and Engineering 6 (2) (2018) 73. doi:10.3390/jmse6020073.

[15] B. Engquist, A. Majda, Absorbing boundary conditions for the numerical simulation of waves, Mathematics of Comp. 31 (139) (1977) 629–651.

[16] R. Higdon, Numerical absorbing boundary conditions for the wave equation, Mathematics of Comp. 49 (179) (1987) 65–95.

[17] D. Givoli, B. Neta, High-order non-reflecting boundary conditions for dispersive waves, Wave Motion 37 (3) (2003) 257 – 271.

[18] B. Düz, R. H. M. Huijsmans, A. E. P. Veldman, M. J. A. Borsboom, P. R. Wellens, An absorbing boundary condition for regular and irregular wave simulations, in: L. Eça, E. Oñate, J. García-Espinosa, T. Kvamsdal, P. Bergan (Eds.), MARINE 2011, IV International Conference on Computational Methods in Marine Engineering: Selected Papers, Springer Netherlands, Dordrecht, 2013, pp. 31–45. doi:10.1007/978-94-007-6143-8_2.

[19] B. Düz, Wave generation, propagation and absorption in CFD simulations of free surface flows, Ph.D. thesis, Delft University of Technology (2015).

[20] Z. Li, G. Deng, P. Queutey, B. Bouscasse, G. Ducrozet, L. Gentaz, D. Le Touzé, P. Ferrant, Comparison of wave modeling methods in CFD solvers for ocean engineering applications, Ocean Engineering 188 (2019) 106237.

[21] H. G. Weller, G. Tabor, H. Jasak, C. Fureby, A tensorial approach to computational continuum mechanics using object orientated techniques, Computers in Physics 12 (6) (1998) 620–631.

[22] H. Jasak, Error analysis and estimation for the finite volume method with applications to fluid flows, Ph.D. thesis, Imperial College, London, UK (1996).

[23] H. Rusche, Computational fluid dynamics of dispersed two-phase flows at high phase fractions, Ph.D. thesis, Imperial College, London, UK (2002).

[24] N. Jacobsen, D. Fuhrman, J. Fredsøe, A wave generation toolbox for the open-source CFD library: OpenFoam, Int. J. for Num. Methods in Fluids 70 (9) (2012) 1073–1088.

[25] S. M. Damiàn, An extended mixture model for the simultaneous treatment of short and long scale interfaces, Ph.D. thesis, Universidad Nacional del Litoral, Santa Fe, Argentina (2013).

[26] Y. Choi, B. Bouscasse, S. Seng, G. Ducrozet, L. Gentaz, P. Ferrant, Generation of regular and irregular waves in Navier-Stokes CFD solvers by matching with the nonlinear potential wave solution at the boundaries, in: ASME 2018 37th Int. C. on Ocean, Offshore and Arctic Eng., 2018, pp. OMAE2018–78077.

[27] C. Monroy, S. Seng, Š. Malenica, Developpements et validation de l'outil CFD OpenFOAM pour le calcul de tenue a la mer, in: 15ème Journées de l'Hydrodynamique, 2016.

[28] C. J. Greenshields, OpenFOAM User Guide, OpenFOAM Foundation Ltd., 2019.

[29] G. Ducrozet, B. Bouscasse, M. Gouin, P. Ferrant, F. Bonnefoy, CN-Stream: Open-source library for nonlinear regular waves using stream function theory, arXiv preprint (2019) arXiv:1901.10577.

[30] J. Allen, Short term spectral analysis, synthesis, and modification by discrete Fourier transform, IEEE Transactions on Acoustics, Speech, and Signal Processing 25 (3) (1977) 235–238. doi:10.1109/TASSP.1977.1162950.

[31] L. Eça, M. Hoekstra, A procedure for the estimation of the numerical uncertainty of CFD calculations based on grid refinement studies, J. of Comp. Physics 262 (2014) 104 – 130.

[32] B. E. Larsen, D. R. Fuhrman, J. Roenby, Performance of interfoam on the simulation of progressive waves, Coastal Engineering Journal 61 (3) (2019) 380–400.

[33] R. Perić, M. Abdel-Maksoud, Analytical prediction of reflection coefficients for wave absorbing layers in flow simulations of regular free-surface waves, Ocean Engineering 147 (2018) 132 – 147. doi:https://doi.org/10.1016/j.oceaneng.2017.10.009.

[34] M. M. Rienecker, J. D. Fenton, A Fourier approximation method for steady water waves, J. of Fluid Mechanics 104 (1981) 119 – 137.

[35] F. Ursell, R. G. Dean, Y. Yu, Forced small-amplitude water waves: a comparison of theory and experiment, Journal of Fluid Mechanics 7 (1960) 33–52.

[36] Y. Goda, T. Suzuki, Estimation of incident and reflected waves in random wave experiments, Coast. Eng. Proc. 1 (1976) 828–845.

[37] L. W. Chew, M. H. Dao, M. Lou, J. Gao, G.-S. J., Wave absorption study of artificial beach with CFD, in: Proc. of the Twenty-fifth (2015) Int. Ocean and Polar Eng. C., 2015, pp. 376–381.

[38] R. A. Carmigniani, D. Violeau, Optimal sponge layer for water waves numerical models, Ocean Engineering 163 (2018) 169 – 182. doi:https://doi.org/10.1016/j.oceaneng.2018.05.068.

[39] C. Monroy, G. Ducrozet, F. Bonnefoy, A. Babarit, L. Gentaz, P. Ferrant, RANS simulations of a CALM buoy in regular and irregular seas using the SWENSE method, International Journal of Offshore and Polar Engineering 21 (4) (2011) 264–271.

[40] R. Perić, M. Abdel-Maksoud, Assessment of uncertainty due to wave reflections in experiments via numerical flow simulations, in: The Twenty-fifth International Ocean and Polar Engineering Conference, 2015, pp. 530–537.

[41] Z. Shen, D. Wan, An irregular wave generating approach based on naoe-FOAM-SJTU solver, China Ocean Eng. 30 (2) (2016) 177–192.

[42] J. M. J. Journée, Theoretical Manual of SEAWAY, TU Delft, Shiphydromechanics Laboratory, Mekelweg 2, 2628 CD Delft, Netherlands, report1216a Edition (Feb. 2001).

[43] F. Ursell, On the heaving motion of a circular cylinder on the surface of a fluid, Quaterly J. of Mechanics and Applied Mathematics 2 (1949) 218–231.

[44] F. Tasai, Formula for calculating hydrodynamic force on a cylinder heaving in free surface (N-parameter family), Tech. Rep. 31, Research Institute for Applied Mechanics, Kyushu University (1960).

[45] F. Tasai, Hydrodynamic force and moment produced by swaying and rolling osciilation of cylinders on the free surface, Tech. Rep. 35, Research Institute for Applied Mechanics, Kyushu University (1961).

[46] J. P. Boris, D. L. Book, Flux-corrected transport. i. shasta, a fluid transport algorithm that works, Journal of Computational Physics 11 (1) (1973) 38 – 69. doi:https://doi.org/10.1016/0021-9991(73)90147-2.